Plastic localization phenomena in a Mn-alloyed austenitic steel

Plastic Localization Phenomena in a Mn-Alloyed Austenitic Steel

G. Scavino[1], F. D'Aiuto[3], P. Matteis[1], P. Russo Spena[2] and D. Firrao[1]

(1) Department of Materials Science and Chemical Engineering (DISMIC), Politecnico di Torino (Torino Technical University), Torino, It, 10129, Italy

(2) Department of Production Systems and Business Economics (DISPEA), Politecnico di Torino (Torino Technical University), Torino, It, 10129, Italy

(3) Engineering & Design, Fiat Group Automobiles, Torino, It, 10135, Italy

D. FirraoFull Professor

Email: donato.firrao@polito.it

Abstract

A 0.5 wt pct C, 22 wt pct Mn austenitic steel, recently proposed for fabricating automotive body structures by cold sheet forming, exhibits plastic localizations (PLs) during uniaxial tensile tests, yet showing a favorable overall strength and ductility. No localization happens during biaxial Erichsen cupping tests. Full-thickness tensile and Erichsen specimens, cut from as-produced steel sheets, were polished and tested at different strain rates. During the tensile tests, the PL phenomena consist first of macroscopic deformation bands traveling along the tensile axis, and then of a series of successive stationary deformation bands, each adjacent to the preceding ones; both types of bands involve the full specimen width and yield a macroscopically observable surface relief. No comparable surface relief was observed

during the standard Erichsen tests. Because the stress state is known to influence PL phenomena, reduced-width Erichsen tests were performed on polished sheet specimens, in order to explore the transition from biaxial to uniaxial loading; surface relief lines were observed on a 20-mm-wide specimen, but not on wider ones.

Manuscript submitted January 22, 2009.

1 Introduction

HIGH manganese austenitic alloys have a remarkable combination of strength and ductility, which makes them interesting for the automotive industry. Steels used for automotive components, such as anti-intrusion bars and structural parts, must display high tensile strength, biaxial ductility, and energy absorption capability for improved fuel saving, crash-test performance, and capability to deep draw complex shapes. High-manganese steels exhibit a better combination of high strength and ductility than most present automotive steels, such as ferritic deep-drawing steels, high-strength low-alloy steels, or multiphase steels. This is due to the mode of deformation: in addition to the dislocation slip mechanism, high-manganese steels also deform by mechanical twinning (this is often called the twinning-induced plasticity, or TWIP, effect), and the twin boundaries behave as obstacles to dislocation movement, similarly to grain boundaries or dislocation forests.

Works have already been performed in alloy development, microstructure analysis, and mechanical properties of TWIP steels;[*1*–*9*] moreover, some recent articles reported the occurrence of plastic instabilities during uniaxial deformation tests;[*10*–*12*] the latter phenomenon was attributed either to plain dynamic strain aging, due to interactions between mobile dislocations and point-defect complexes including interstitial C atoms,[*10*] or to not yet clarified, more complex atomic interactions, also involving twinning phenomena.[*11*]

In the present article, the mechanism of plastic deformation of a batch produced 1.5-mm-thick TWIP sheet steel (with 0.5 pct C) has been studied in-depth, with the purpose of describing and explaining the occurrence of plastic instabilities, with both uniaxial and biaxial deformation experiments. To investigate plastic instabilities, several tensile tests were performed at low to medium crosshead speeds, thus varying the applied strain rates, accordingly. Moreover, standard and reduced-width Erichsen tests were done to investigate the influence of biaxial stresses on plastic instabilities.

2 Experimental Procedures

The chemical composition of the TWIP steel is reported in Table I. Manganese is the main alloy element and stabilizes the austenitic matrix at room temperature; carbon is employed to increment the yield and tensile strength by interstitial solute hardening.

The microstructural characterization was carried out both by scanning electron microscopy (SEM, with the electron channeling contrast technique), after electrochemical etch, and by optical microscopy, after nital or picral etch. The austenitic average grain size was determined by using the circular intercept method[*13*] on optical microscopy images, after picral etch. Macro- and microhardness Vickers tests were performed on virgin material to evaluate the occurrence of mechanical inhomogeneities.

Full-thickness tensile flat specimens (80-mm gage length, 20-mm width) and Erichsen both standard (100 × 100 mm) and reduced width (10 × 100, 20 × 100, and 30 × 100 mm) test pieces were cut from as-produced TWIP steel sheets. The tensile specimens were oriented in the rolling direction. All the tests were performed at room temperature.

The Erichsen cupping tests (on both standard and reduced width specimens) were performed by using the proprietary "OKS 200," Mo_2S-based, lubricant paste, which was evenly applied on the specimen area in contact with the punch.

Tensile tests were carried out under displacement control, by a servohydraulic testing system controlled at four different crosshead speeds, namely, 0.05, 0.5, 5, and 39 mm/s. During each test, different strain rates, in the 0.0003 to 0.0005 s^{-1}, 0.003 to 0.005 s^{-1}, 0.03 to 0.05 s^{-1}, and 0.2 to 0.4 s^{-1} ranges, respectively, were achieved.

The specimens were mirror polished before the mechanical tests in order to observe the transient macroscopic specimen surface relief due to plastic instabilities (this was recorded by a video camera during the tensile tests) and to examine, thereafter, both the residual surface relief and the deformed microstructure without further preparation, to avoid artifacts.

In order to facilitate the observation of the transient surface relief, most tensile tests were performed without extensometers; thus, in several instances, the engineering stress-strain curves were derived from the recorded crosshead displacement, instead of from the extensometer signal, by using the following procedure. First, the crosshead displacement was corrected by subtracting the displacement due to the estimated elastic compliance of the load frame and of the specimen end grips (even if this correction was relevant only before the specimen yielding). Then, the engineering stress s was calculated as usual and the engineering strain e was calculated as the corrected crosshead displacement divided by an effective specimen length (equal to 108 mm), which was found by a trial and error procedure, by comparing the engineering stress-strain curves of the same test obtained either from the crosshead displacement or from the extensometer displacement. This effective length was employed because not only the 80-mm

gage length, but also the specimen end regions (having a large fillet radius) were significantly deformed during the tests. Finally, the true stress σ and strain ε were calculated from the engineering ones with the usual formulas, as if the specimen deformation had been homogeneous (*i.e.*, by neglecting the localized deformation phenomena); hence, the true stress and true strain values are spatial averages.

Lateral surface X-ray diffraction analyses were performed before and after the tensile tests, to reveal second phases (occurring in detectable amount) as well as the possible occurrence of deformation-induced martensitic transformations. SEM analysis was also performed on the fracture surfaces of tensile samples.

3 Results

The optical microscope and SEM observations and the X-ray diffraction analyses show that the as-received TWIP steel consists of homogeneous and isotropic austenite grains, with an average size of about 3 μm (Figure 1); thus, the material was fully recrystallized after (or during) the final sheet forming operations. However, the metallographic etch (nital and picral) of sheet cross sections allows detection of a banding contrast, superimposed to the aforementioned homogeneous and isotropic grain-boundary network (Figure 1(b)); these bands are attributed to small compositional segregations arising from the solidification process and elongated in the rolling direction.

The X-ray analysis did not detect any phases other than austenite; it allows us to conclude that the formation of the M_3C carbides foreseen by the Fe-C-Mn ternary phase diagram at temperatures below 600 °C[*14*] was probably suppressed by the thermomechanical process; however, the presence of sub-micron-sized alloy carbides (*e.g.*, VC) cannot be completely ruled out. The very fine grain size was probably due to the contribution of both the thermomechanical process and the grain-refining effect of V.

All the as-received samples have a similar Vickers hardness, about 290 HV_{100}. No significant microhardness difference was detected on the sheet cross section; thus, it is concluded that the production process does not yield sensible mechanical inhomogeneities in the sheet thickness.

The engineering and true stress-strain curves of the examined steel are plotted in Figure 2, and the corresponding tensile properties are listed in Table II, as a function of the crosshead speed; the average (estimated) strain rate of each test is also reported in the same table. It is confirmed that the TWIP steel exhibits a remarkable combination of strength and ductility, with a large and almost constant strain hardening slope, as previously noted in high-Mn steels.[*1*,*2*]

The yield strength of the TWIP steel does not vary significantly with the crosshead speed in the examined range, with values around 550 MPa. As a contrast, as the crosshead speed is increased from 0.05 to 39 mm/s, the strain hardening

slope and the pointwise flow stress (Figure 2) slightly decrease. Finally, rupture elongation displays the largest values at intermediate crosshead speeds.

Stress-strain curves exhibit smooth or serrated regions as a function of strain and of crosshead speed, thus revealing different plastic behaviors. The serrations are attributed to plastic localization (PL) effects, which are also evidenced during the test by macroscopic specimen surface relief lines, either transient or permanent. No such effects were detected in the tensile test carried out at 39 mm/s crosshead speed, showing a smooth stress-strain curve.

On the contrary, at crosshead speeds equal or lower than 5 mm/s, and starting from a critical engineering strain e_c (or true strain ε_c), successive macroscopic bands appear on the surface on the tensile specimen, forming angles of about 55 deg with the tensile axis and involving the entire section of the specimen; these bands are defined here as type I bands. These bands spread through the specimen length, a new one being nucleated as the previous reaches one specimen grip end, continuously repeating the same mechanism. Contemporaneously, the stress-strain curve detected by the displacement gage shows a series of steps, each corresponding to the transit of a band through the gage length (Figure 3), and the stress-strain curve detected by the crosshead displacement shows isolated stress peaks (Figure 2), each immediately preceding the nucleation of a new band. Afterward, and up to rupture, a series of stationary deformation bands appears, giving off distinctive sharp noises, forming angles of about 55 deg with the tensile axis, most being immediately adjacent to the preceding ones; these are defined here as type II bands.

As the crosshead speed increases from 0.05 to 5 mm/s, the critical point e_c (or ε_c) at which type I bands start increases from 0.17 to 0.44 engineering strain (or 0.16 to 0.37 true strain), and these bands travel faster and faster throughout the tensile samples.

To enhance the visibility of the effects of the propagation of the type I bands, an enlarged portion of the true stress–true strain curve of the 0.05 mm/s crosshead speed test, recorded by the use of a 25-mm gage extensometer, is shown in Figure 3(a). Successive short plastic flows at quasi-constant stress are evident: they take place when a type I band crosses the gage measurement zone (Figure 3(b)) and are followed by a steep stress increase, until a successive type I band travels through the gage zone, repeating the same pattern. In Figure 3(a), a series of light lines having a slope equal to the steel elastic modulus are superimposed to these stress steps, showing that the slope of the true tensile curve recorded by the strain gage can be at times equal to the elastic modulus, although it is generally lower than that.

Enlarged portions of the stress-strain curves, during the occurrence of type II bands, are displayed in Figure 4(a). In this case, no strain gage was mounted and the sample overall strain was measured by means of the crosshead displacement transducer. When a type II band appears, the tensile stress suddenly drops at almost constant strain (in order to maintain the imposed crosshead speed). The type II bands are evident on tensile specimens as permanent crossed macroscopic

surface relief lines (Figure 4(b)). Careful examination of the stress-strain curves (Figure 2) reveals that the amplitude of the stress drops, associated with type II bands, overall increases with the crosshead speed.

As a function of crosshead speed, the tensile specimen failed in different ways (Figure 5): at the lower tested crosshead speed, the fracture was almost orthogonal to the tensile axis, whereas at the highest crosshead speeds, it generally occurred at an angle of approximately 45 deg with respect to the tensile axis, sometimes with a small central orthogonal fracture zone and with oblique lateral regions (with either equal or opposite slope, due to the equal occurrence probability of α and β macroscopic slip line theory characteristic lines, as described in Reference *10*).

SEM investigations of fractured tensile samples show surface steps (on the previously polished lateral surfaces, Figure 6(a)) with spacing of tenths of micrometers, which are limited by the (deformed) grain boundaries; these are probably traces of either mechanical twins or slip planes.

The tensile specimen fracture surfaces (Figure 6(b)) are completely ductile (neither cleavage nor intergranular rupture is present) with very small dimples, consistent with the fine microstructure of the as-received steel. The fracture surface morphology does not change within the examined tensile test's crosshead speed range.

The X-ray diffraction measurements performed on the as-received sheet and on the deformed steel after a tensile test (crosshead speed 0.1 mm/s) are compared in Figure 7. No peaks ascribable to bct-martensite or hcp-martensite are observed. On the other hand, both the intensity and the width of the peaks are changed by the test due to the reorientation of the austenite crystal structure.

The standard Erichsen tests were performed with different average punch speeds v_p. When the punch displacement is equal to the punch radius r_p (10 mm), the shape of the specimen's deformed region can be approximated by a hemisphere and the (true) linear strain in the sheet plane can be defined as $0.5 \cdot \ln(A_1/A_0) \approx 0.35$, where $A_1 = 2\pi \cdot r_p^2$ is the area of the aforementioned hemisphere, and $A_0 = \pi \cdot r_p^2$ is the area of the punch projection on the undeformed sheet. Therefore, the (true) strain rate and the (true) strain at rupture occurring during the reported standard Erichsen test can be roughly estimated as $0.35/(r_p/v_p)$ and $0.35 \cdot (E_i/r_p)$, where E_i is the Erichsen index. The standard Erichsen test results are reported in Table III (results of the test performed with the maximum punch speed are affected by a larger uncertainty), with the strain rates and strains at fracture estimated by this method. No macroscopic surface relief was detected during these tests; moreover, no serrations were detected in the acquired force-displacement curves.

The reduced-width Erichsen tests were performed at the lowest available punch speed. All the specimens were broken close to the border of the clamping dies. No transient macroscopic surface relief was detected visually during these tests. The successive analysis of the fractured specimens, performed at low magnification with a light microscope, revealed a series of parallel surface relief lines in the 20-mm-wide specimen (Figure 8), although in one region only (close to the final rupture) out of four possible symmetrical ones. These surface relief lines form a ~45 deg angle with

the longer specimen side, which is also the main apparent local deformation direction. No analogous features were detected in the other specimens; however, the 10-mm-width specimen exhibited, on a large part of its deformed area, surface marks due to slide through the clamping dies, which could easily have hindered any possible surface relief due to PLs.

4 Discussion

Irregular plastic flow was shown to occur while tensile testing TWIP steel sheets in a certain range of strain and strain rates at room temperature. Chakrabarti and Spretnak[15] showed that PLs (other than necking) as a general rule can occur when the following constitutive equation is satisfied:

$$\frac{\partial \sigma}{\partial \varepsilon}\delta\varepsilon + \frac{\partial \sigma}{\partial \dot{\varepsilon}}\delta\dot{\varepsilon} + \frac{\partial \sigma}{\partial T}\delta T \leq 0$$

In the adiabatic plastic deformation case (in which the temperature rise due to localized plastic deformation induces thermal softening, which in turn decrease the local flow stress and thus allows further localized deformation), this condition is achieved by a relatively large negative thermal contribution $(d\sigma/dT)\delta T$ upon raising the temperature by adiabatic heating, the other contributions being positive but lower than the thermal one. Due to heat flow considerations, adiabatic instabilities normally occur at very large (ballistic) strain rates, much larger than those examined here.[15] When adiabatic instabilities were previously observed in AISI 4340 steel at moderate strain rates, they were allowed by the very low strain hardening slope of the quenched and tempered steel,[16,17] whereas in the present steel, the strain hardening is comparatively higher. Moreover, due to the same heat flow considerations, adiabatic instabilities should be favored by increasing strain rates,[15] whereas in the present case, the opposite holds. Therefore, the possible thermal contribution to the present PLs should be limited.

Plastic localization behaviors similar to the present one were previously observed in other alloys and referred to as “serrated flow” or “repetitive yielding” or “jerky flow,” and have been often attributed to the Portevin–Le Chatelier (PLC) effect.[18] In these cases, the unstable plastic flow is due to a decrease of the flow stress with increasing applied strain rate,[18] *i.e.*, to a large negative $d\sigma/d\varepsilon$ term in the previous constitutive equation, whereas the stress-strain curve still displays positive strain hardening;[18] this phenomenon is often called *negative strain-rate sensitivity* or *strain-rate softening*. In these PLC cases, the thermal softening contribution may be negligible; for example, previous tests on Al-Mg alloys showed temperature increases associated with room-temperature PLC effects of the order of 5 °C or less.[19] It has been clarified[20,21] that repeated dislocation pinning by interstitial solute elements is a necessary condition to produce a negative strain rate sensitivity and, hence, macroscopically visible PLC serrations in tensile stress-strain

curves. During the waiting time spent at obstacles, glide dislocations are subjected to an additional pinning by solute atoms diffusing toward the dislocations, so that the obstacle strength increases as the waiting times increase due to a low macroscopic strain rate. The negative strain rate sensitivity arises because larger macroscopic strain rates correspond to smaller dislocation waiting times and hence to lower solute-pinning effects.[*18*]

The plastic instabilities appear as surface bands propagating throughout the specimen, which may be stationary (type C bands) or may travel along the tensile axis, either through the whole specimen length (type A bands) or only through part of it (type B bands), as defined in Reference *18*. Moreover, C bands can occur in series, each being immediately ahead of the previous one in the same tensile axis direction, so that the overall phenomenon can still be interpreted as a PL front moving along the specimen axis, even if by discrete steps, rather than continuously advancing throughout the specimen.[*22*]

The overall negative strain rate sensitivity of the TWIP steel, and the nature of the type I and type II PL bands during the tensile tests performed at 0.04 s^{-1} or at lower strain rates (5 mm/s or lower crosshead speeds) in the same steel, as described previously, are both consistent with the occurrence of a PLC effect in the TWIP steel; in this regard, the type I and type II PL bands described previously are recognized as type A and type C PLC bands. Type B deformation bands were not unequivocally detected by macroscopic transient surface relief observations, but were probably present during the transition between type A and C bands in the above described TWIP steel tensile specimens; such a hypothesis is also supported by the comparison of the *s-e*serration shape in the transition from A to C bands with previous results.[*22*]

Further tensile tests will be necessary in order to define the exact threshold strain rate above which the PLC effect disappears; from the preceding results, it is possible to conclude that in the present steel such a threshold is comprised between 0.04 and 0.3 s^{-1} uniaxial strain rate (5 and 39 mm/s crosshead speed in the present tests series).

The previously described dislocation pinning by interstitial solute elements, occurring during the test, which is also named dynamic strain aging, is hypothesized to be the primary mechanism inducing the PLC effect in this alloy; however, the exact nature of the interaction between mobile dislocations and solute atoms is still controversial and other mechanisms causing PLC effects are proposed in the literature.[*10*,*11*,*23*,*24*]

The present results and interpretation regarding the occurrence of type A PLC bands during room-temperature tensile tests are in overall agreement with some recent observations concerning C-alloyed TWIP steels;[*10*–*12*] on the contrary, the occurrence of type C PLC bands was not reported in the same articles.

Since the strain localization associated with the PLC effect replicates (as opposed to the Lüders bands, which occur only at first yield), it cannot be suppressed by predeformation (skin pass): surface markings and waviness of aesthetic concern may be expected during sheet forming operations due to inhomogeneous plastic deformation.

The full-width Erichsen test results confirm the negative strain rate sensitivity of the present steel, since the force at rupture (which is positively correlated with the maximum flow stress value) significantly decreases with increasing strain rate. However, no PLs were observed in the slowest full-width Erichsen tests (*i.e.*, those performed with the smaller punch speeds, Table III) even if they satisfied, in each strain direction, the uniaxial strain and strain rate conditions that induced PLs in tensile tests (Table II); only in the faster Erichsen tests could the absence of PLs be ascribed to the strain rate being too high, or the strain to fracture being too low. Therefore, it should be concluded that the biaxial stress state has an impeding effect upon the occurrence of PL phenomena. This conclusion is consistent with the results of the reduced-width Erichsen tests, in which the stress state becomes less and less biaxial with decreasing testpiece width. In fact, no surface relief lines were detected in the 30-mm-width test, and only very shallow (*i.e.*, much less evident than those observed in the tensile tests) ones were observed in the 20-mm-width tests. Therefore, on the basis of these results, the PLC effect is not expected to significantly deteriorate the surface quality of sheet-formed components, since these are often subjected to significantly biaxial stress states.

It should be noted that, even at the higher examined strain rate, which promotes the absence of plastic instabilities and of aesthetically detrimental marks, the strength and ductility combination of the TWIP steel is still remarkable in respect to other steel grades employed in deep drawing applications.

Finally, the absence of martensite after the room-temperature tensile tests, assessed by the XRD analyses, can be related to the examined steel stacking fault energy (SFE). Remy and Pineau[*25*] reported deformation-induced martensitic transformations in a 20 pct Mn, 4 pct Cr, 0.5 pct C austenitic steel at temperatures equal or lower than 32 °C, with SFE having been determined as equal to 11 mJ/m^2; thus, it can be hypothesized that the present steel has a somewhat higher SFE than that, which is consistent with previous observations that the SFE of high-Mn austenitic steels increases with both the Mn and C content and decreases with the Cr content.[*5*] This is also consistent with the finding that deformation-induced martensitic transformations occur in a 25 pct Mn austenitic steel with less than 0.05 pct C only at temperatures lower than –70 °C,[*2*] since in this latter case the much lower C content further decreases the SFE value.

5 Summary And Conclusions

The overall plastic behavior of an austenitic high manganese carbon steel has been examined by using different strain and stress rates on both uniaxial tensile specimens and biaxial Erichsen cupping testpieces. Erichsen tests were performed either on standard or on reduced-width specimens. The following remarks can be made.

1. The TWIP steel exhibits PLs during uniaxial tensile tests for strain rates lower than 0.3 s^{-1}. These plastic instabilities are due to a PLC effect, and in particular they are probably caused by the observed negative strain-rate sensitivity (decreasing the flow stress with increasing strain rate). The plastic instabilities appear as easily visible successive surface bands; the first bands travel throughout the specimen length (type A bands), whereas

the stationary bands (type C bands) appear later and up to the final fracture. As the strain rate of the tensile test increases from 0.0004 to 0.04 s^{-1}, the critical deformation at which type A bands appear increases from 0.17 to 0.44 engineering strain (or 0.16 to 0.37 true strain), and these bands travel faster throughout the tensile samples.

2. The standard Erichsen test results are consistent with a negative strain rate sensitivity of the TWIP steel, since the force at rupture, and hence the maximum flow stress value, significantly decreases with increasing strain rate. However, no macroscopic localization happens during these tests; thus, the biaxial stress state prevents the PL phenomena. This is consistent with the observation of few surface relief lines at low magnification on a 20-mm-width Erichsen specimen, since its stress state is less biaxial.

3. On the basis of X-ray diffraction analyses, performed before and after the tensile tests, no deformation-induced martensitic transformations occur during the deformation of the austenitic microstructure. The absence of martensite is consistent with an estimated rather high SFE.

Acknowledgments

ArcelorMittal steelwork for steel procurement. P. Iulita, Fiat Auto Engineering & Design, for the SEM microstructural analysis. C. Pozzi, Politecnico di Torino, for the X-ray analyses. G.M.M. Mortarino, Politecnico di Torino, for collaboration in tensile testing and for useful discussion.

References

1. O. Grässel and G. Frommeyer: *Mater. Sci. Technol.*, 1998, vol. 14, pp. 1213–16.

2. O. Grässel, L. Kruger, G. Frommeyer, and L.W. Meyer: *Int. J. Plasticity*, 2000, vol. 16, pp. 1391–1409.MATHCrossRef

3. P. Yang, Q. Xie, L. Meng, H. Ding, and Z. Tang: *Scripta Mater.*, 2006, vol. 55, pp. 629–31.CrossRef

4. S. Vercammen, B. Blanpain, B.C.D. Cooman, and P. Wollants: *Acta Metall.*, 2004, vol. 52, pp. 2005–12.

5. O. Bouaziz and N. Guelton: *Mater. Sci. Eng. A*, 2001, vols. 319–321, pp. 246–49.

6. S. Allain, J.P. Chateau, and O. Bouaziz: *Mater. Sci. Eng. A*, 2004, vols. 387–389, pp. 143–47.

7. S. Allain, J.P. Chateau, and O. Bouaziz: *Steel Res.*, 2002, vol. 73, pp. 299–302.

8. D. Cornette, P. Cugy, A. Hildenbrand, Bouzekri, and G. Lovato: *Rev. Metall.*, 2005, Dec., pp. 905–18.

9. G. Frommeyer, U. Brux, and P. Neumann: *ISIJ Int.*, 2003, vol. 43, pp. 438–46.CrossRef

10. J.K. Kim, L. Chen, H.S. Kim, S.K. Kim, G.S. Kim, Y. Estrin, and B.C. De Cooman: *Steel Res. Int.*, 2009, vol. 80, pp. 493–98.

11. T.A. Lebedkina, M.A. Lebyodkin, J.P. Chateau, A. Jacques, and S. Allain: *Mater. Sci. Eng. A*, 2009, vol. 519, pp. 147–54.CrossRef

12. P.D. Zavattieri, V. Savic, L.G. Hector, J.R. Fekete, W. Tong, and Y. Xuan: *Int. J. Plasticity*, 2009, vol. 25, pp. 2298–2330.CrossRef

13. ASTM E112-96, *Standard Test Methods for Determining Average Grain Size*, ASTM International, West Conshohocken, PA, 1996. DOI:10.1520/E0112-96R04E02

14. G.V. Raynor and V.G. Rivlin: *Phase Equilibria in Iron Ternary Alloys*, The Institute of Metals, London, 1988, pp. 168–76.

15. A.K. Chakrabarti and J.W. Spretnak: *Metall. Trans. A*, 1975, vol. 6A, pp. 733–36.ADS

16. A.K. Chakrabarti and J.W. Spretnak: *Metall. Trans. A*, 1975, vol. 6A, pp. 737–47.ADS

17. J.W. Spretnak and D. Firrao: *Metall. Ital.*, 1980, vol. 72, pp. 525–34.

18. E. Rizzi and P. Häner: *Int. J. Plasticity*, 2004, vol. 20, pp. 121–65.MATHCrossRef

19. H. Louche, P. Vacher, and R. Arrieux: *Mater. Sci. Eng. A*, 2005, vol. 404, pp. 188–96.CrossRef

20. P. Hahner: *Mater. Sci. Eng. A*, 1996, vol. 207, pp. 208–16.CrossRef

21. M. Zaiser and P. Hahner: *Phys. Status Solidi B*, 1997, vol. 199, pp. 267–330.CrossRefADS

22. L.J. Cuddy and W.C. Leslie: *Acta Metall.*, 1972, vol. 20, pp. 1157–67.CrossRef

23. Y.N. Dastur and W.C. Leslie: *Metall. Trans. A*, 1981, vol. 12A, pp. 749–59.ADS

24. W.S. Owen and M. Grujicic: *Acta Mater.*, 1999, vol. 47, pp. 111–26.CrossRef

25. L. Remy and A. Pineau: *Mater. Sci. Eng.*, 1977, vol. 28, pp. 99–107.

TABLES

Table I. Chemical Composition of the TWIP Steel (Weight Percent)

C	Mn	Mo	V	Si	Cr	P	S
0.50	22.4	0.70	0.22	0.16	0.13	0.025	<0.001

Table II. Results of Tensile Tests with Increasing Crosshead Speeds; Average Strain Rate, Yield Stress (YS), Ultimate Tensile Stress (UTS), Strain Hardening Slope (dσ/dε) Calculated from the Linear Interpolation of the True Stress-Strain Curves between σ ≈ 600 MPa and ε ≈ 0.35, Engineering (e_c) and True (ε_c) Strains at the Onset of PL Phenomena, and Total Elongation (Et); Strains Calculated from Crosshead Displacements

Crosshead Speed (mm/s)	Strain Rate (Average) (s^{-1})	Mean Value ± Standard Deviation							Individual Test Results						
		YS (MPa)	UTS (MPa)	$d\sigma/d\varepsilon$ (MPa)	e_c (Pct)	ε_c (Pct)	E_t (Pct)		YS (MPa)	UTS (MPa)	$d\sigma/d\varepsilon$ (MPa)	e_c (Pct)	ε_c (Pct)	E_t (Pct)
0.05	0.0004	551 ± 3	1178 ± 11	2870 ± 40	24 ± 5	21 ± 4	61 ± 5	*	553	1184	2928	17	16	56
									549	1187	2857	30	26	67
									554	1178	2858	25	23	59
									549	1163	2838	23	21	63
0.5	0.004	541 ± 1	1118 ± 11	2737 ± 5	32 ± 5	27 ± 4	61	*	540	1126	2733	28	25	61
									541	1110	2740	35	30	61
5	0.04	548 ± 4	1093 ± 5	2695 ± 23	44 ± 2	36 ± 1	58 ± 5	*	552	1099	2716	44	37	63
									546	1087	2664	46	38	62
									542	1095	2694	41	34	52
									550	1092	2706	45	37	56
39	0.3	557	1063	2620	—	—	49	*	557	1063	2620	not observed		49

*Tests shown in Figures 2 through 6.

Table III. Standard Erichsen Test Results

Average Punch Speed, v_p (mm/s)	Estimated Strain Rate (s^{-1})	Erichsen Index, E_i (mm)	Force at Rupture (kN)	Estimated True Strain at Rupture (—)
0.04	0.001	11.47	88	0.40
0.44	0.015	11.90	83	0.41
1.00	0.035	10.96	78	0.38
2.35	0.081	9.39	64	0.33

FIGURES

Fig. 1—Austenitic microstructure. Optical microscopy after picral etch: (a) sheet surface and (b) longitudinal cross section. SEM after electrochemical etch (transverse cross section): (c) overview and (d) detail.

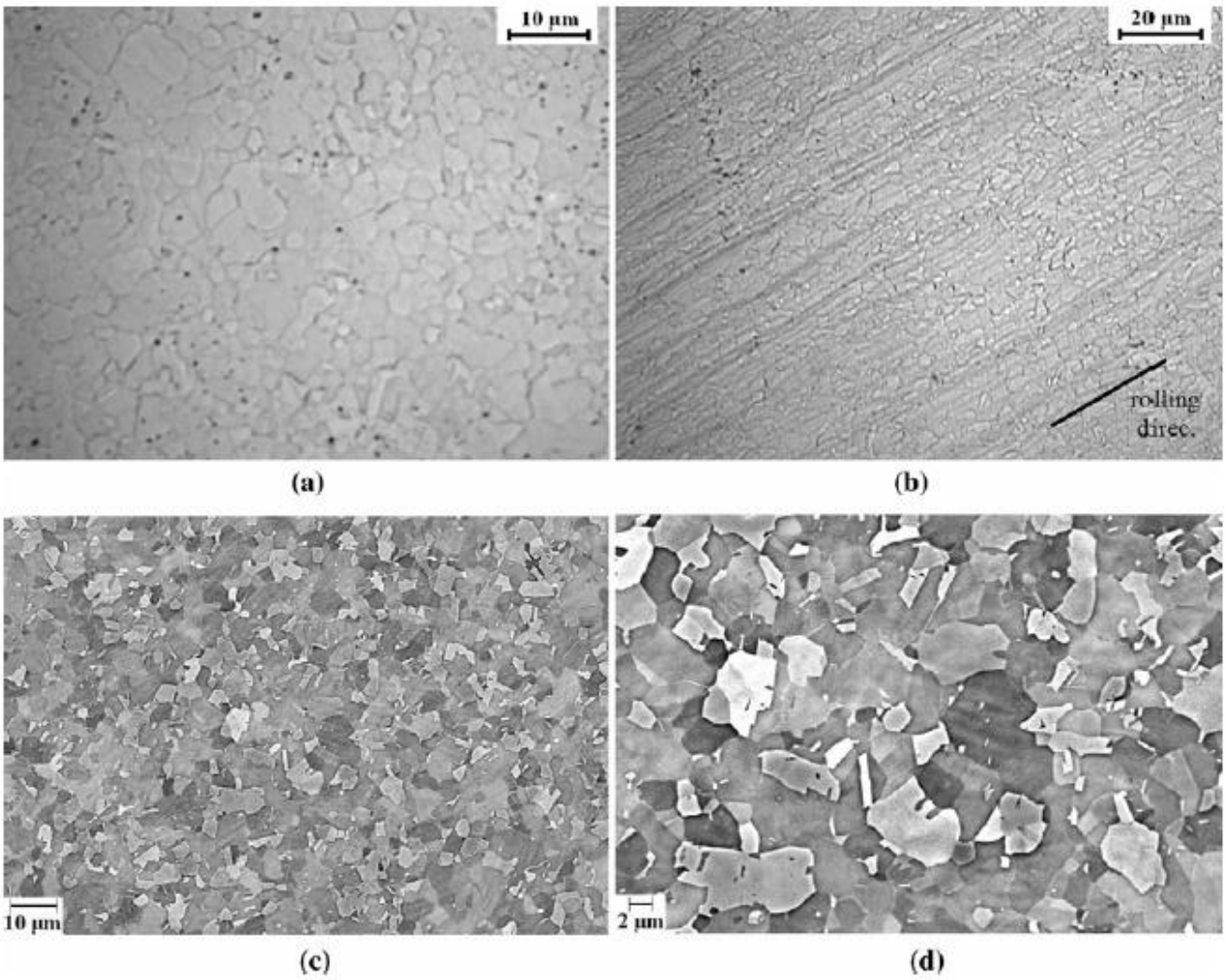

Fig. 2—Engineering and true stress-strain curves and onset of the PL effect (●) as a function of crosshead speed. No PL effect for the 39 mm/s crosshead speed. Strain calculated from crosshead displacement.

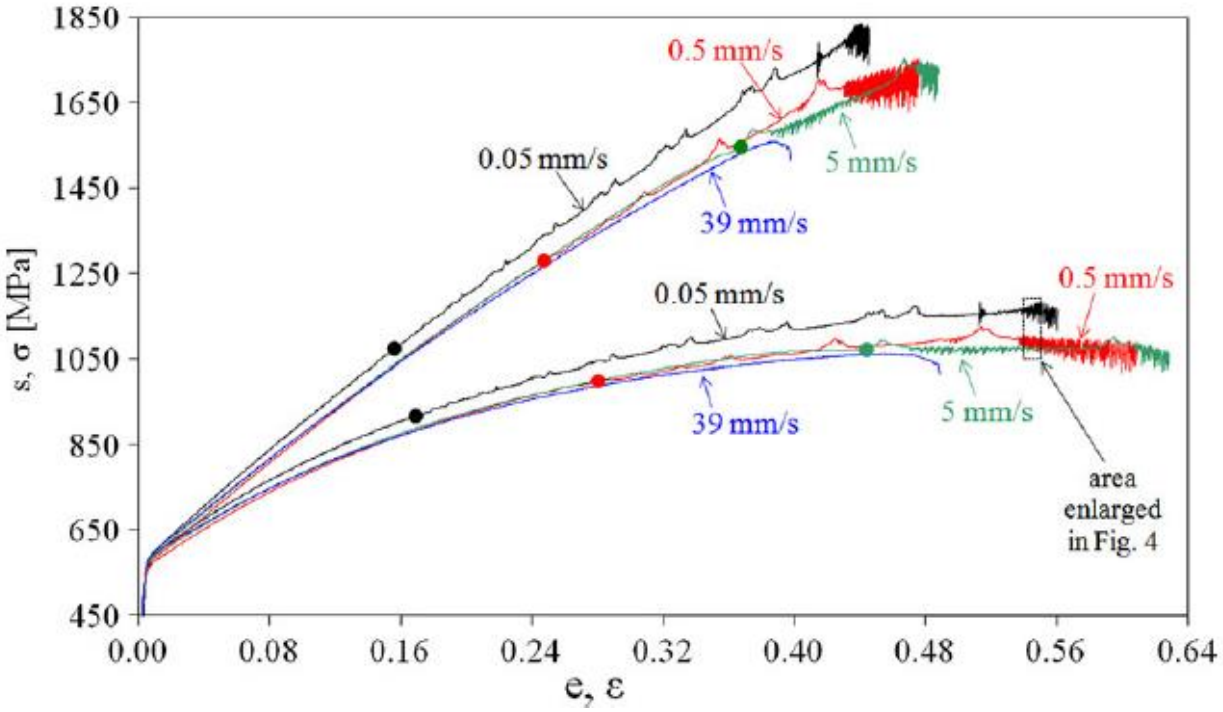

Fig. 3—(a) True stress-strain curve calculated from the gage displacement (the strain gage was removed after ~0.4 true strain); (b) enlarged portion with type I serrations, superimposed to lines having a slope equal to the elastic modulus; and (c) type I band in the gage measurement zone. Crosshead speed: 0.05 mm/s.

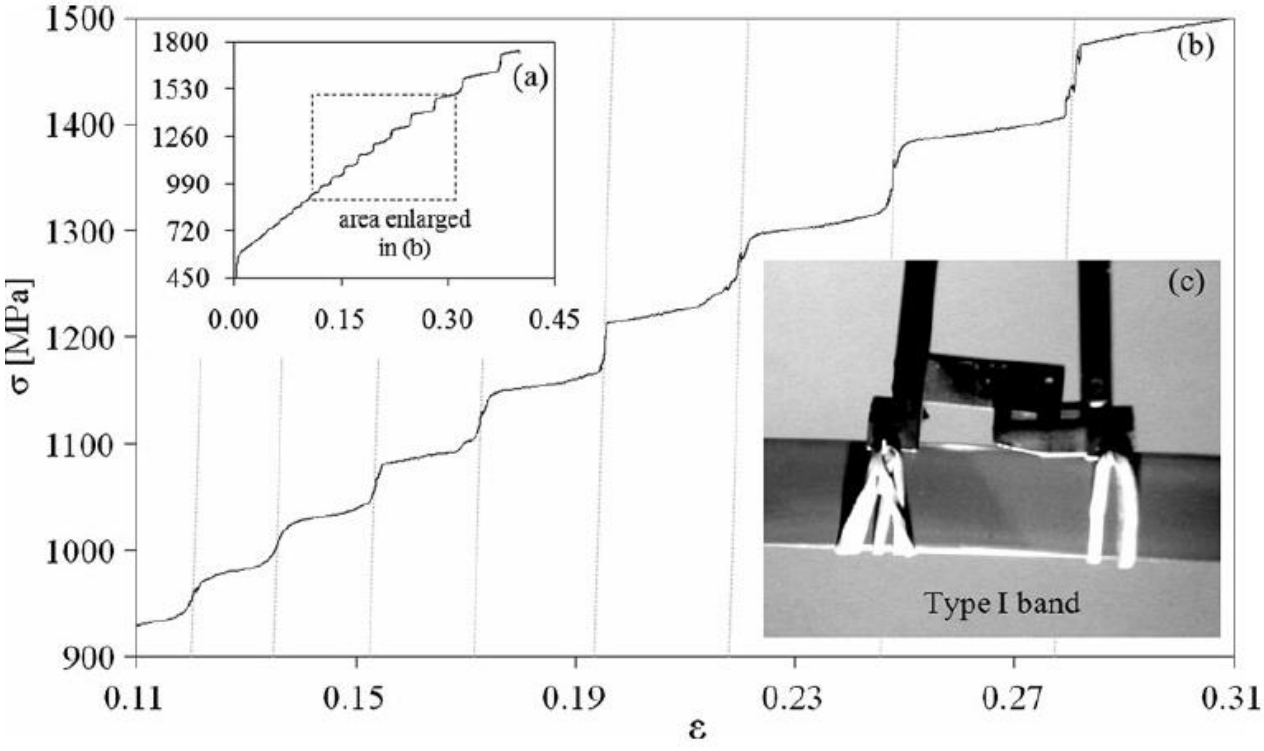

Fig. 4—(a) Effect of the type II serrations in the engineering stress-strain curve. (b) Type II bands on the tensile specimen. Strain calculated from the crosshead displacement.

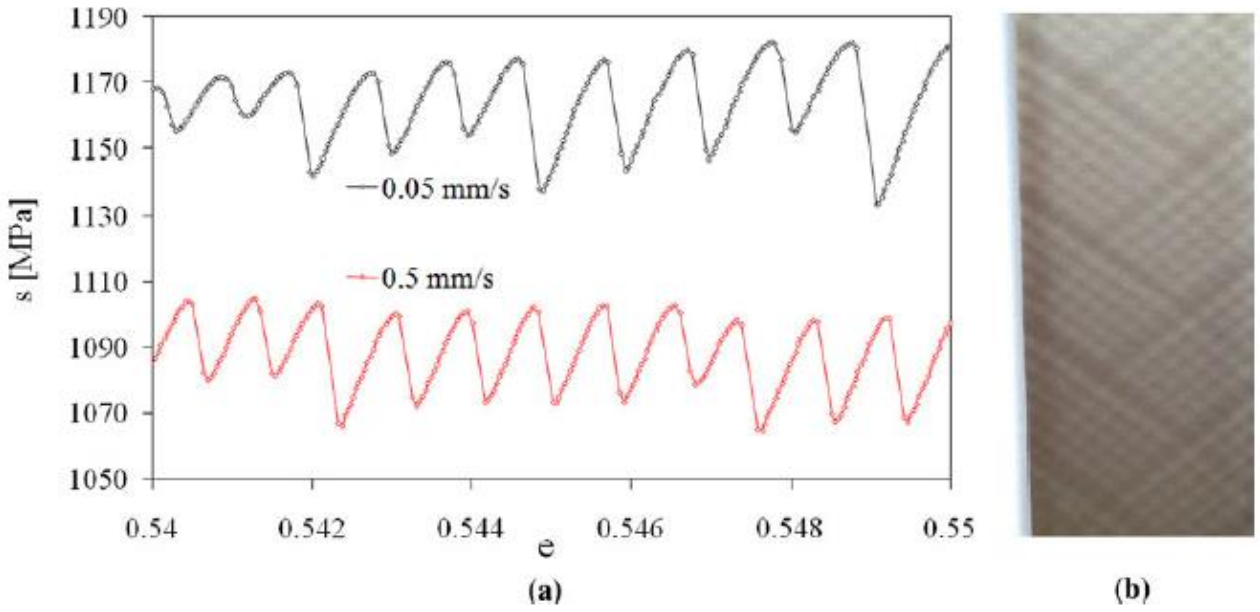

Fig. 5—Macroscopic fracture shape as a function of the crosshead speed.

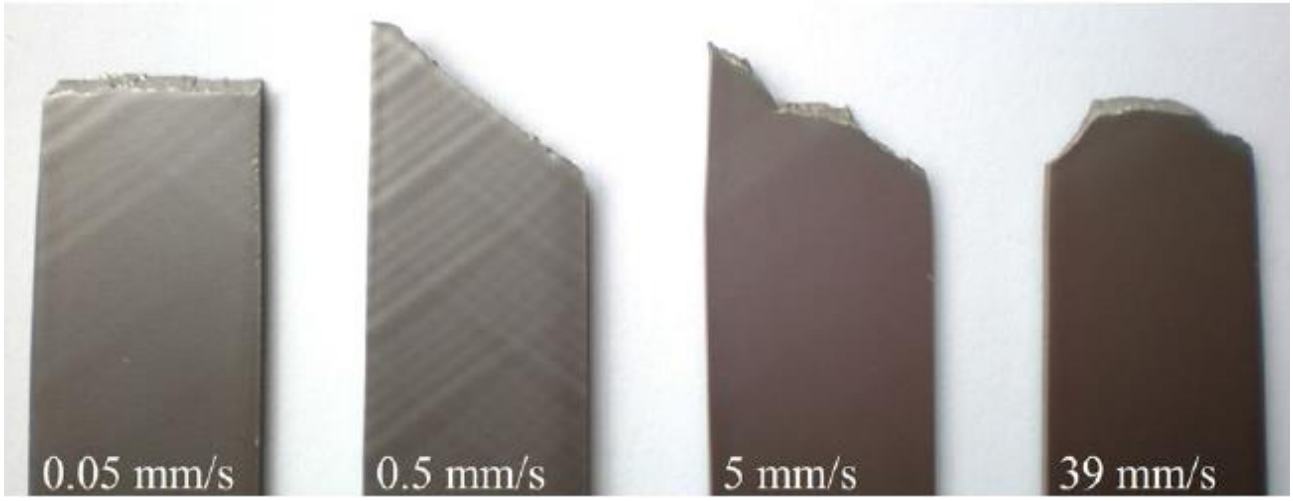

Fig. 6—SEM analysis. Microscopic deformation steps on the (a) previously polished surface and (b) tensile fracture surface after the tensile test at 0.05 mm/s crosshead speed.

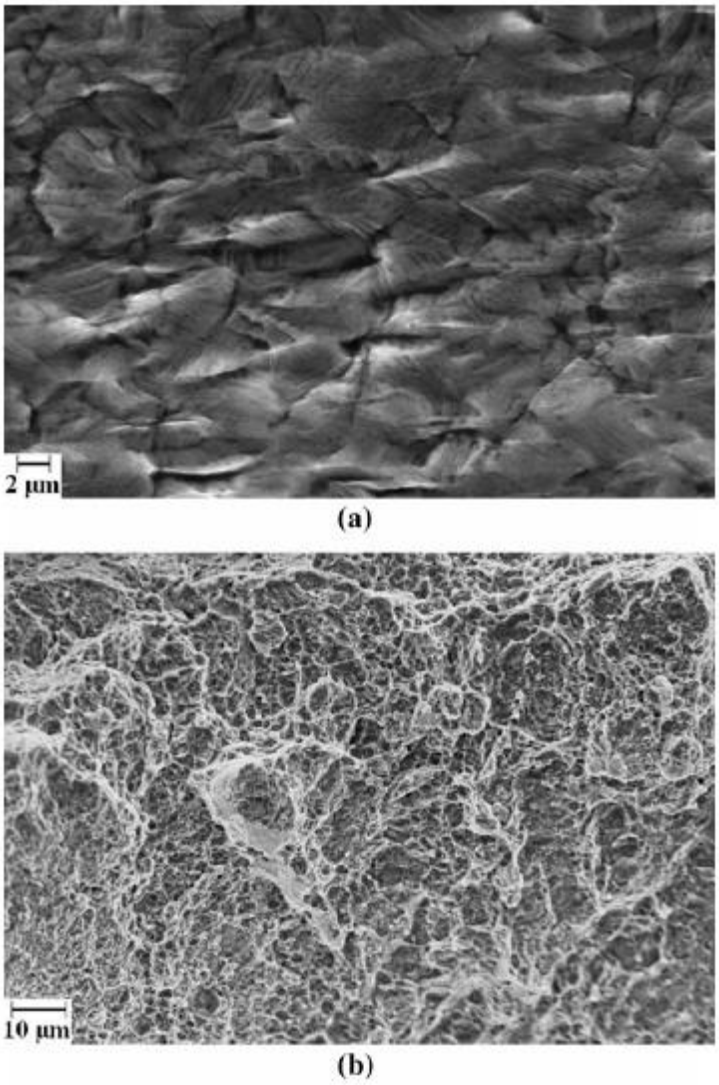

Fig. 7—Diffractograms of the TWIP steel (a) before and (b) after tensile tests. Co Kα radiation.

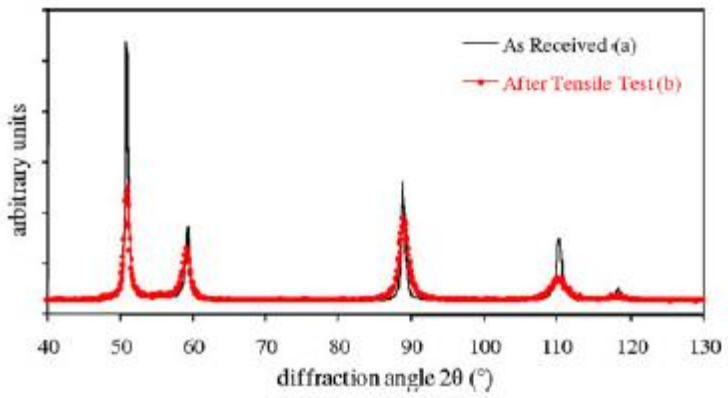

Fig. 8—(a) Surface relief lines on part of the previously polished surface of the 20 x 100 mm reduced-width Erichsen testpiece. (b) Approximate position of the pictured area on the broken specimen.